The Astrophysical Journal, 943:94 (12pp), 2023 February 1 https://doi.org/10.3847/1538-4357/aca89a

The Low-redshift Lyman Continuum Survey: Optically Thin and Thick Mg II Lines as Probes of Lyman Continuum Escape

Xinfeng Xu[1], Alaina Henry[1,2], Timothy Heckman[1], John Chisholm[3], Rui Marques-Chaves[4], Floriane Leclercq[3], Danielle A. Berg[3], Anne Jaskot[5], Daniel Schaerer[4], Gábor Worseck[6], Ricardo O. Amorín[7], Hakim Atek[8], Matthew Hayes[9], Zhiyuan Ji[10], Göran Östlin[9], Alberto Saldana-Lopez[4], and Trinh Thuan[11]
[1] Center for Astrophysical Sciences, Department of Physics & Astronomy, Johns Hopkins University, Baltimore, MD 21218, USA; xinfeng@jhu.edu
[2] Space Telescope Science Institute, 3700 San Martin Drive, Baltimore, MD 21218, USA
[3] Department of Astronomy, The University of Texas at Austin, 2515 Speedway, Stop C1400, Austin, TX 78712, USA
[4] Department of Astronomy, University of Geneva, 51 Chemin Pegasi, 1290 Versoix, Switzerland
[5] Department of Astronomy, Williams College, Williamstown, MA 01267, USA
[6] Institut für Physik und Astronomie, Universität Potsdam, Karl-Liebknecht-Str. 24/25, D-14476 Potsdam, Germany
[7] Instituto de Investigacion Multidisciplinar en Ciencia y Tecnologia, Universidad de La Serena, Raul Bitran 1305, La Serena, Chile
[8] Institut d'astrophysique de Paris, CNRS, Sorbonne Université, 98bis Boulevrad Arago, F-75014, Paris, France
[9] Department of Astronomy, Oskar Klein Centre; Stockholm University; SE-106 91 Stockholm, Sweden
[10] University of Massachusetts Amherst, 710 North Pleasant Street, Amherst, MA 01003-9305, USA
[11] Astronomy Department, University of Virginia, Charlottesville, VA 22904, USA
Received 2022 October 13; revised 2022 November 28; accepted 2022 December 1; published 2023 January 27

Abstract

The Mg II $\lambda\lambda$2796, 2803 doublet has been suggested as a useful indirect indicator for the escape of Lyα and Lyman continuum (LyC) photons in local star-forming galaxies. However, studies to date have focused on small samples of galaxies with strong Mg II or strong LyC emission. Here, we present the first study of Mg II to probe a large dynamic range of galaxy properties, using newly obtained high-signal-to-noise, moderate-resolution spectra of Mg II, for a sample of 34 galaxies selected from the Low-redshift Lyman Continuum Survey. We show that the galaxies in our sample have Mg II profiles ranging from strong emission to P-Cygni profiles to pure absorption. We find that there is a significant trend (with a possibility of spurious correlations of $\sim$2%) that galaxies that are detected as strong LyC emitters (LCEs) show larger equivalent widths of Mg II emission, while non-LCEs tend to show evidence of more scattering and absorption features in Mg II. We then find that Mg II strongly correlates with Lyα in both equivalent width and escape fraction, regardless of whether emission or absorption dominates the Mg II profiles. Furthermore, we show that, for galaxies that are categorized as Mg II emitters, one can use the information of Mg II, metallicity, and dust to estimate the escape fraction of LyC within a factor of $\sim$3. These findings confirm that Mg II lines can be used as a tool for selecting galaxies as LCEs and thus serve as an indirect indicator for the escape of Lyα and LyC.

Unified Astronomy Thesaurus concepts: Galaxy evolution (594); Reionization (1383); Optical astronomy (1776); Emission line galaxies (459)

1. Introduction

Over the last decades, considerable observational efforts have been directed toward studying the escape of Lyman continuum (LyC) photons from galaxies and attempting to explain the last phase transition of the universe, i.e., cosmic reionization. Various publications have pointed out that star-forming (SF) galaxies can be responsible for the epoch of reionization (EoR). These include studies of low-redshift galaxies ($z \lesssim 1$; e.g., Heckman et al. 2001; Bergvall et al. 2006; Leitet et al. 2013; Borthakur et al. 2014; Izotov et al. 2016a, 2016b; Leitherer et al. 2016; Puschnig et al. 2017; Izotov et al. 2018a, 2018b; Wang et al. 2019; Chisholm et al. 2020; Izotov et al. 2021; Wang et al. 2021; Marques-Chaves et al. 2022a; Flury et al. 2022a, 2022b; Chisholm et al. 2022; Izotov et al. 2022; Saldana-Lopez et al. 2022; Xu et al. 2022), as well as moderate- to high-redshifted galaxies ($z \sim 2$–4; e.g., Robertson et al. 2015; de Barros et al. 2016; Shapley et al. 2016; Vanzella et al. 2016; Bian et al. 2017; Marchi et al. 2017, 2018; Steidel et al. 2018; Vanzella et al. 2018; Fletcher et al. 2019; Rivera-Thorsen et al. 2019; Ji et al. 2020; Mestrić et al. 2020; Vielfaure et al. 2020; Begley et al. 2022; Marques-Chaves et al. 2022b; Naidu et al. 2022; Rivera-Thorsen et al. 2022). These galaxies are proposed to be analogs of high-redshift ($z \sim$ 6–8) ones at EoR (e.g., Schaerer et al. 2016; Boyett et al. 2022).

Due to the attenuation by Lyman limit systems and/or the neutral intergalactic medium (IGM), it is challenging to detect LyC photons at $z \gtrsim 5$ (Inoue et al. 2014; Worseck et al. 2014; Becker et al. 2021; Bosman et al. 2022). Therefore, various indirect indicators have been developed from lower-redshift analogs (see the summary in Flury et al. 2022a, 2022b). One of the leading indicators is the Lyα emission (e.g., Henry et al. 2015; Verhamme et al. 2015; Dijkstra et al. 2016; Verhamme et al. 2017; Jaskot et al. 2019; Gazagnes et al. 2020; Kakiichi & Gronke 2021; Izotov et al. 2022). Given the resonance nature of Lyα, the escape of Lyα photons contains information about the neutral hydrogen in/around the galaxy, and leaves footprints on the Lyα emission line profiles (e.g., Izotov et al. 2018b; Gazagnes et al. 2020; Flury et al. 2022b; Le Reste et al. 2022). Nonetheless, since Lyα photons can also be absorbed by the neutral IGM, the interpretation of Lyα profiles

for high-z galaxies ($z \gtrsim 4$) is nontrivial (e.g., Stark et al. 2011; Schenker et al. 2014; Gronke et al. 2021; Hayes et al. 2021).

The Mg II $\lambda\lambda$2796, 2803 doublet has been commonly detected as a pair of absorption lines in galaxies, which trace the galactic outflows and their feedback effects (e.g., Weiner et al. 2009; Erb et al. 2012; Finley et al. 2017; Wang et al. 2022). Recently, however, Mg II has been found to show strong doublet emission lines in galaxies that are classified as LyC emitter (LCE) candidates. Various publications have suggested that the escape of Mg II correlates with that of Lyα and LyC in SF galaxies (Henry et al. 2018; Chisholm et al. 2020; Izotov et al. 2022; Naidu et al. 2022; Seive et al. 2022; Xu et al. 2022).

Mg II emission was studied by Henry et al. (2018) in a sample of 10 compact SF galaxies. For the first time, they showed that the escape of Mg II correlates with the escape of Lyα. This result is interpreted as evidence that both Mg II and Lyα photons escape from galaxies through a similar path of low–column density gas. Indeed, Chisholm et al. (2020) point out that the flux ratios between the doublet lines of Mg II [i.e., F(Mg II 2796)/F(Mg II 2803); hereafter, R] can be used to trace the column density of neutral hydrogen. They and Xu et al. (2022) combined the Mg II emission, metallicity, and dust attenuation to predict $f_{\rm esc}^{\rm LyC}$, and found that the predicted $f_{\rm esc}^{\rm LyC}$ correlates with the observed $f_{\rm esc}^{\rm LyC}$ in samples of galaxies with strong Mg II emission lines. Xu et al. (2022) also found that the galaxies selected with strong Mg II emission lines might be more likely to leak LyC than similar galaxies with weaker Mg II. In an independent sample, Izotov et al. (2022) confirmed that escaping LyC emission is detected predominantly in galaxies with $R \gtrsim 1.3$, which indicates that the optical depth of Mg II is low (i.e., $\tau_{2803} \lesssim 0.5$; Chisholm et al. 2020). Therefore, a high R ratio can be used to select LCE candidates.

Mg II emission lines are also detected in higher-redshift SF galaxies. For example, in the stacks of bright Lyα emitters (LAEs) at $z \sim 2$, Naidu et al. (2022) found that LCE candidates tend to have R close to 2, while the Mg II emission is closer to the systemic velocity (instead of being redshifted in non-LCEs). In addition, Witstok et al. (2021) found in a lensed $z \sim 5$ galaxy that the escape of Mg II photons is consistent with that of Lyα. However, Katz et al. (2022) pointed out from hydro-cosmological simulations that Mg II is only a useful diagnostic of $f_{\rm esc}^{\rm LyC}$ in the optically thin regime.

Though all of these studies support the hypothesis that strong Mg II emission lines and a high R ratio can serve as a good indirect indicator for Lyα and LyC escape, there exist two caveats. (1) Existing samples are commonly small and only focus on SF galaxies with strong Mg II emission lines and/or galaxies as strong LCEs. The latter also result in substantial Mg II emission lines. Similar SF galaxies with Mg II as weaker emission lines, P-Cygni profiles, or absorption lines have not been systematically studied in observations. (2) Some of these studies only have low-signal-to-noise (S/N) Mg II spectra (e.g., Izotov et al. 2022; Naidu et al. 2022; Xu et al. 2022). Their determinations of R, and the subsequent inference of the Mg II optical depth, have more scatter, due to the low-S/N spectra.

In this paper, we further study Mg II as an indirect indicator for the escape of Lyα and LyC, while we also attempt to mitigate the two caveats noted above. We focus on galaxies from the Low-redshift Lyman Continuum Survey (LzLCS; Flury et al. 2022a), where a large sample of 66 LCE candidates are selected without reference to their Mg II emission lines. For 34 of the 66 LzLCS galaxies, we present ground-based follow-up spectroscopy of the Mg II feature. These data provide a higher spectral resolution and S/N than the Sloan Digital Sky Survey (SDSS)/BOSS, along with coverage of Mg II in galaxies where it is blueward of the SDSS bandpass. As we will show, these data achieve more secure measurements of the Mg II properties, ultimately validating the use of Mg II as an indirect indicator for the escape of Lyα and LyC.

The structure of the paper is as follows. In Section 2, we introduce the observations, data reduction, and basic measurements of the optical emission lines. In Section 3, we show how we derive various important parameters from the observed Mg II doublet. We present the main results in Section 4, including the comparisons of Mg II with Lyα and LyC. We conclude the paper in Section 5.

2. Observations, Data Reductions, and Basic Analyses

2.1. UV Spectra for LyC and Lyα Regions

In this study, we focus on LCE candidates from LzLCS (Flury et al. 2022a), which contains 66 SF galaxies at $z \sim 0.3$. The survey obtained rest-frame UV spectra for each galaxy, with the G140L grating on the Hubble Space Telescope/Cosmic Origins Spectrograph (HST/COS), under program GO 15626 (PI: Jaskot). Both LyC and Lyα regions have been covered. The detailed data reductions of the G140L data, as well as the analysis of the Lyα and LyC escape, are presented in Flury et al. (2022a). In this paper, we adopt their derived quantities for LyC and Lyα. These mainly include their escape fractions and the equivalent widths (EWs) for Lyα.

2.2. Optical Spectra for Mg II Regions

The galaxies in the LzLCS sample already have SDSS or BOSS spectra, where the blue wavelength coverages end at 3800 Å and 3650 Å, respectively. Thus, the Mg II features are only observed by SDSS or BOSS for galaxies with $z \gtrsim 0.35$ or 0.30, respectively. Even for the cases with existing Mg II spectra from SDSS/BOSS, as discussed in Xu et al. (2022), the S/Ns of the intrinsically weak Mg II lines and the spectral resolutions ($\sim$1500) are commonly too low. In this case, the measurements of Mg II, especially R, have large error bars. Therefore, we have obtained higher-S/N and higher–spectral resolution observations for 34 galaxies from the LzLCS sample. These galaxies are observed by the Multiple Mirror Telescope (MMT), the Very Large Telescope (VLT), or the Hobby–Eberly Telescope (HET). In this paper, we focus on studying the Mg II properties from this subsample of 34 galaxies. The observation details and data reductions are listed in Table 1 and discussed below.

2.2.1. MMT Observations and Data Reductions

A total of 24 galaxies from the LzLCS sample have been observed by MMT. We adopt the blue channel spectrograph, using a 1″ slit with the 832 lines mm^{-1} grating at the second order. This leads to a spectral resolution of $\sim$1 Å ($\sim$90 km s^{-1} near the Mg II region). The observations were conducted on six nights in three different semesters (2019A, 2020A, and 2021A). The exposure time was between 30 and 180 minutes, depending on the brightness of the target (Table 1). We stay toward lower airmass ($\lesssim$1.3) and, for every exposure, we reset the slit at the parallactic angle. We reduce the data following the methodology described in Henry et al. (2018),

Table 1
Follow-up Observations and Basic Properties for the Galaxies in Our Sample

ID	R.A.	Decl.	z[a]	Instrument[b]	Date[c] (yyyy/mm/dd)	Exp.[c] (s)	SDSS-u[d] (mag)	$E(B-V)_{MW}$[e]	$E(B-V)_{int.}$[f]
J0957+2357	09:57:00	+23:57:09	0.2444	MMT/Blue	2019/04/08	4800	18.42	0.0287	0.3007
J1314+1048	13:14:19	+10:47:39	0.2960	MMT/Blue	2019/04/08	3600	19.69	0.0371	0.1621
J1327+4218	13:26:33	+42:18:24	0.3176	MMT/Blue	2019/04/08	3600	20.48	0.0173	0.1641
J1346+1129	13:45:59	+11:28:48	0.2371	MMT/Blue	2019/04/08	3600	19.00	0.0231	0.2022
J1410+4345	14:10:13	+43:44:35	0.3557	MMT/Blue	2019/04/08	7200	21.70	0.0196	0.1413
J0926+3957	09:25:52	+39:57:14	0.3141	MMT/Blue	2019/04/09	7200	21.27	0.0270	0.1364
J1130+4935	11:29:33	+49:35:25	0.3448	MMT/Blue	2019/04/09	7200	21.50	0.0292	0.0446
J1133+4514	11:33:04	+65:13:41	0.2414	MMT/Blue	2019/04/09	7200	20.14	0.0158	0.0886
J1246+4449	12:46:19	+44:49:02	0.3220	MMT/Blue	2019/04/09	4800	20.48	0.0200	0.1595
J0723+4146	07:23:26	+41:46:08	0.2966	MMT/Blue	2020/02/19	7200	20.89	0.0467	0.0097
J0811+4141	08:11:12	+41:41:46	0.3329	MMT/Blue	2020/02/19	7200	21.17	0.0383	0.1150
J1235+0635	12:35:19	+06:35:56	0.3326	MMT/Blue	2020/02/19	6000	20.72	0.0333	0.0782
J0814+2114	08:14:09	+21:14:59	0.2271	MMT/Blue	2020/02/20	1800	18.91	0.0336	0.1800
J0912+5050	09:12:08	+50:50:09	0.3275	MMT/Blue	2020/02/20	9600	20.56	0.0245	0.1088
J1301+5104	13:01:28	+51:04:51	0.3476	MMT/Blue	2020/02/20	2500	20.04	0.0222	0.0974
J0047+0154	00:47:43	+01:54:40	0.3535	MMT/Blue	2021/01/09	3600	20.28	0.0312	0.1760
J0826+1820	08:26:52	+18:20:52	0.2972	MMT/Blue	2021/01/09	7200	21.35	0.0328	0.0300
J1158+3125	11:58:55	+31:25:59	0.2430	MMT/Blue	2021/01/09	2700	19.27	0.0226	0.1037
J1248+1234	12:48:35	+12:34:03	0.2635	MMT/Blue	2021/01/09	6900	20.16	0.0519	0.0627
J0113+0002	01:13:09	+00:02:23	0.3060	MMT/Blue	2021/01/10	7200	20.56	0.0312	<1E-4
J0129+1459	01:29:10	+14:59:35	0.2799	MMT/Blue	2021/01/10	4800	20.11	0.0688	0.0729
J0917+3152	09:17:03	+31:52:21	0.3003	MMT/Blue	2021/01/10	3300	19.78	0.0204	0.1920
J1033+6353	10:33:44	+63:53:17	0.3465	MMT/Blue	2021/01/10	2700	19.84	0.0160	0.0819
J1038+4527	10:38:16	+45:27:18	0.3256	MMT/Blue	2021/01/10	2700	19.40	0.0241	0.2506
J0036+0033	00:36:01	+00:33:07	0.3480	VLT/X-Shooter	2020/11/05	2800	21.83	0.0278	0.2007
J0047+0154	00:47:43	+01:54:40	0.3537	VLT/X-Shooter	2020/10/23	5500	20.28	0.0312	0.0699
J0113+0002	01:13:09	+00:02:23	0.3062	VLT/X-Shooter	2020/10/23	5500	20.56	0.0312	0.1144
J0122+0520	01:22:17	+05:20:44	0.3655	VLT/X-Shooter	2020/10/23	5500	21.38	0.0559	0.1166
J0814+2114	08:14:09	+21:14:59	0.2271	VLT/X-Shooter	2020/12/21	2800	18.91	0.0335	0.1984
J0911+1831	09:11:13	+18:31:08	0.2622	VLT/X-Shooter	2021/01/16	2800	19.79	0.0279	0.1106
J0958+2025	09:58:38	+20:25:08	0.3016	VLT/X-Shooter	2021/02/04	2800	19.86	0.0347	0.0650
J1310+2148	13:10:37	+21:48:17	0.2830	VLT/X-Shooter	2021/04/10	5500	20.40	0.0204	0.0924
J1235+0635	12:35:19	+06:35:56	0.3327	VLT/X-Shooter	2022/01/12	5500	20.72	0.0333	0.0782
J1244+0215	12:44:23	+02:15:40	0.2394	VLT/X-Shooter	2022/03/08	2800	19.56	0.0424	0.0673
J0834+4805	08:34:40	+48:05:41	0.3425	HET/LRS2	2021/12/30	5400	20.62	0.0383	0.1741
J0940+5932	09:40:01	+59:32:44	0.3716	HET/LRS2	2022/01/24	5400	20.80	0.0380	0.4158
J1517+3705	15:17:07	+37:05:12	0.3533	HET/LRS2	2022/07/22	6300	20.87	0.0411	0.0005
J1648+4957	16:48:49	+49:57:51	0.3818	HET/LRS2	2022/05/27	5400	21.93	0.0374	0.0070

Notes.
[a] The redshift of the objects derived from fitting the Balmer emission lines.
[b] The instruments that are used for the follow-up observations (Section 2.2).
[c] The observation start date and exposure time in seconds, respectively.
[d] The *u*-band magnitudes from SDSS photometry.
[e] The Milky Way dust extinction obtained from the Galactic Dust Reddening and Extinction Map (Schlafly & Finkbeiner 2011), at the NASA/IPAC Infrared Science Archive.
[f] The internal nebular dust extinction of the galaxy derived from the Balmer lines (Section 2.3).

using IDL + IRAF routines. The wavelength calibration is applied from the HeArHgCd arc lamps. By matching the arc lines, we find that the rms of the residuals is < 0.1 Å ($\sim$10 km^{-1} around the Mg II spectral regions).

Given the short wavelength coverage of the blue channel spectrograph in MMT ($\sim$3100–4100 Å), the only major line covered is the Mg II doublet. Therefore, we also adopt SDSS/BOSS spectra to measure other optical lines (Section 2.3). For each galaxy, we calculate its *u*-band magnitude from the MMT spectra and scale it to the galaxy's *u*-band magnitude from the SDSS photometry. This accounts for any slit losses between the MMT and SDSS observations.

2.2.2. VLT Observations and Data Reductions

We also include 10 LzLCS sources, observed by the X-Shooter spectrograph mounted on the VLT, as part of ESO program ID 106.215K.001 (PI: Schaerer). The observations were carried out between 2020 fall and 2022 spring. We use 1.″0, 0.″9, and 0.″9 slits in the UVB, VIS, and NIR arms, providing resolution powers of $\sim$5400, 8900, and 5600,

respectively. This yields a spectral resolution of $\sim$50 km s^{-1} near the Mg II regions. Observations were performed in nodding-on-slit mode, with a standard ABBA sequence and total on-source exposure times of 46 minutes or 92 minutes, depending on the brightness of each source (Table 1). We reduce the X-Shooter data following the methods in Marques-Chaves et al. (2022a), adopting the standard ESO Reflex reduction pipeline (version 2.11.5; Freudling et al. 2013).

For each galaxy, we also calculate the u-band magnitude from the VLT spectra and match it to the galaxy's u-band magnitude from the SDSS photometry. Four of our galaxies are observed by both MMT and VLT. We have checked that the Mg II spectral profiles from the two telescopes are similar, and that the Mg II line flux ratios (i.e., R) are consistent within errors. This is expected, since the galaxies in our sample are rather compact (with UV half-light radii $\lesssim 0.''4$) and are smaller than the slit sizes. Finally, we adopt the VLT observations of these galaxies in our analyses, given their higher S/Ns.

2.2.3. HET Observations and Data Reductions

We include four additional galaxies from the LzLCS sample, which are observed by the Low-Resolution Spectrograph 2 (LRS2) on HET (Ramsey et al. 1998). LRS2 is an integral field spectrograph with nearly complete spatial sampling and a native spatial scale of $0.''25 \times 0.''25$ spaxels, with an average of $1.''25$ seeing (Chonis et al. 2016). LRS2 has a wavelength coverage from 3600 Å to 10000 Å, and its spectral resolution around the Mg II region is 1.63 Å. To match our MMT and VLT slit sizes, we extract the Mg II spectra in the central $1.''0 \times 1.''0$ aperture. We reduce the LRS2 data using the same methods as in Seive et al. (2022), where we adopt the HET LRS2 pipeline, Panacea,[12] to perform the initial reductions, including fiber extraction, wavelength calibration, astrometry, and flux calibration. For each galaxy, we also calculate the u-band magnitude from the LRS2 spectra and match it to the galaxy's u-band magnitude from the SDSS photometry.

2.2.4. Summary of Optical Spectra

Overall, we obtain higher-quality data for 34 of the 66 galaxies from the LzLCS sample. We show the finally reduced Mg II spectra for these galaxies in Figures 1 and 2, and we order them by the decreasing absolute escape fraction of LyC ($f_{\rm esc}^{\rm LyC}$), as measured from fitting the UV continuum (reported in Flury et al. 2022a). Based on their LyC measurements, these galaxies have an $f_{\rm esc}^{\rm LyC}$ range between 0% and 30%. Of the 34 galaxies, 20 are classified as LCEs (sometimes referred to as LyC "leakers"), which have LyC fluxes detected with 97.725% confidence (Flury et al. 2022a). The other 12 galaxies are classified as non-LCEs. We show the derived $f_{\rm esc}^{\rm LyC}$ values in the top left corner of each panel, while we present the $f_{\rm esc}^{\rm LyC}$ upper limits for non-LCEs. We mark the galaxies that were observed by X-Shooter or LRS2 with an extra "X" or "L," respectively, at the end of the object names in Figures 1 and 2.

2.3. Measurements of Optical Emission Lines

For the galaxies that have new optical spectra, as described above, we measure several optical emission lines whenever they are covered, including Mg II, [O II], [O III], and Balmer lines. For each galaxy, we first correct the spectra for Milky Way extinction, using the Galactic Dust Reddening and Extinction Map (Schlafly & Finkbeiner 2011) at the NASA/IPAC Infrared Science Archive, assuming the extinction law from Cardelli et al. (1989). The redshift of the galaxy is matched to the peak of the Balmer emission lines.

We determine the continuum flux for the Mg II spectral region by adopting a linear fit to the spectra $\sim \pm 2000$ km s^{-1} around the systemic velocity. We then split the spectra at the midpoint between the two lines, i.e., 2799.1 Å, to represent the spectral regions for Mg II 2796 and 2803 separately. For each Mg II line, we also split it into absorption (below the continuum) and emission (above the continuum) parts. After this, we integrate the separate spectral regions, to get the flux and the EW. The corresponding errors on these quantities are estimated through a Monte Carlo simulation, where we perturb the spectrum 10^4 times, according to the observed 1σ uncertainties. These values are reported in Table 2. Note that we do not correct the Mg II line fluxes by the internal dust extinction of the galaxy. This is because the Mg II photons are resonantly scattered, like Lyα, and robust correction is difficult (Henry et al. 2018; Chisholm et al. 2020; Xu et al. 2022).

For the other optical lines, we measure their flux and EW in a similar way as for Mg II. However, unlike Mg II, since they are not resonant lines, we also correct the spectra by the internal dust extinction for the galaxy, before the measurements. The internal dust extinction ($E(B-V)_{\rm int.}$) for each galaxy is measured from the Balmer lines, following the methods in Xu et al. (2022). For galaxies that only have new MMT observations, because the MMT blue channel does not cover the Balmer lines, we adopt $E(B-V)_{\rm int.}$, as derived in Flury et al. (2022a), based on their SDSS spectra. The final $E(B-V)_{\rm int.}$ values are reported in the final column in Table 1.

In Figure 3, we compare the subsample adopted in this paper (red) to the rest of the galaxies in LzLCS (gray). We show two general observables that can be measured at high redshift, including O32 = the flux ratio of [O III] λ5007/[O III] λ3727 and the stellar mass derived from the spectral energy distribution (SED) fitting reported in Flury et al. (2022a). Our subsample of galaxies is randomly selected from the LzLCS parent sample, to ensure a large dynamic range in galaxy properties.

3. Analyses

In this section, we present the methodology for deriving important properties from Mg II lines. We first discuss the significant trends in the Mg II line profiles in Section 3.1. We then show the plausible geometry for Mg II photon escape in Section 3.2. We present the methods for deriving the Mg II escape fractions ($f_{\rm esc}^{\rm MgII}$) from photoionization models in Section 3.3. Finally, we discuss how to predict the LyC escape fraction ($f_{\rm esc,pd}^{\rm LyC}$) from Mg II, metallicity, and dust attenuation in Section 3.4.

3.1. Significant Trends of the Mg II Line Profiles

In Figures 1 and 2, we show the Mg II spectra of our galaxies in order of decreasing $f_{\rm esc}^{\rm LyC}$, as derived from the HST/COS G140L spectra (Flury et al. 2022a). There exists a significant trend, in that galaxies that are detected as strong LCEs also show strong Mg II emission lines, while non-LCEs present more absorption features in Mg II. We apply the Kendall τ test between EW(Mg II) and $f_{\rm esc}^{\rm LyC}$, where we have considered the

[12] https://github.com/grzeimann/Panacea

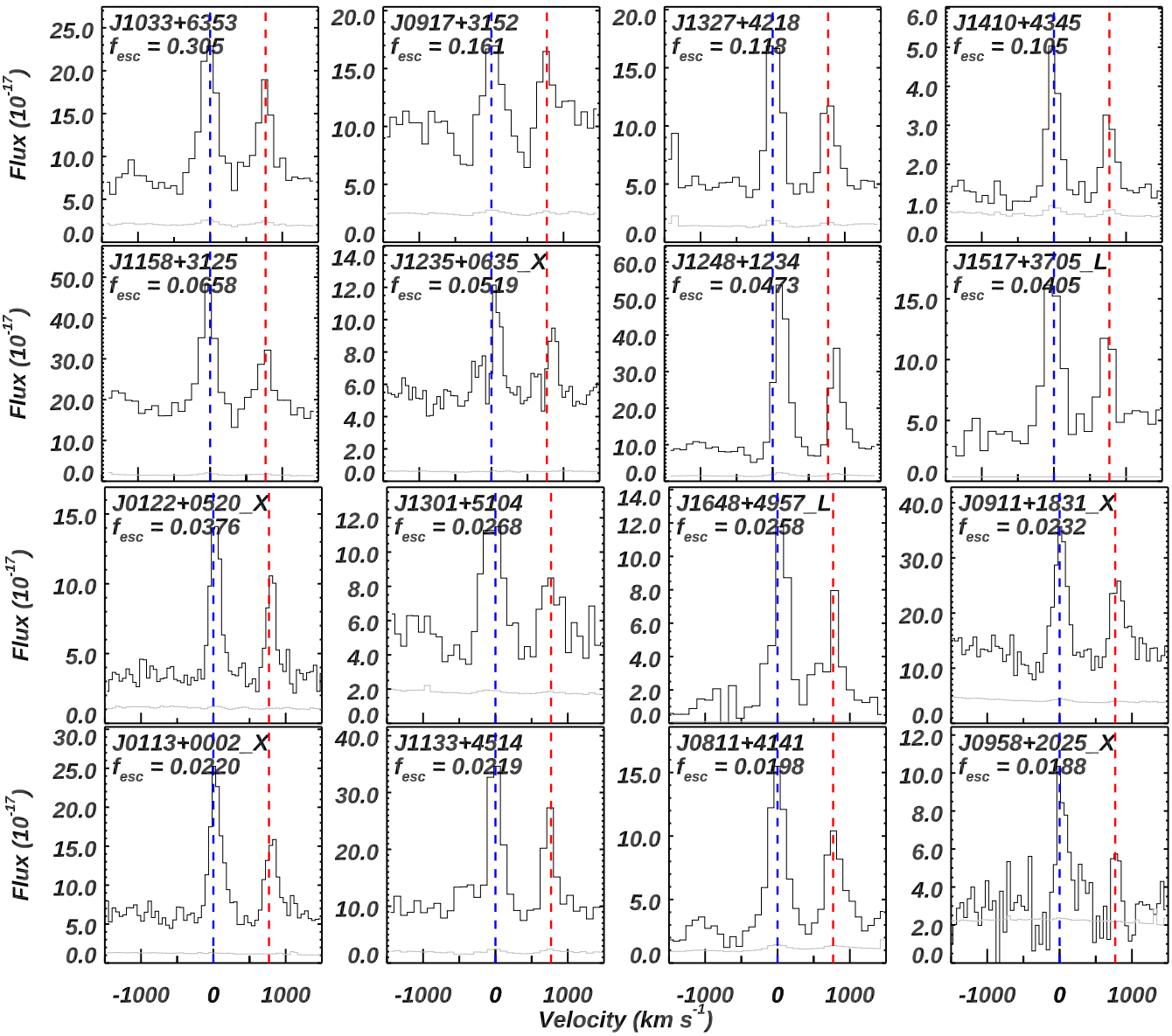

Figure 1. The finally reduced Mg II spectra for LzLCS galaxies in velocity space, with data taken from either the MMT blue channel spectrograph or the VLT/X-Shooter spectrograph. For the X-Shooter and LRS2 observations, we give an extra "X" or "L," respectively, at the end of the object names. The *y*-axes are in units of 10^{-17} ergs s^{-1} cm^{-2} Å^{-1}. The data and corresponding errors are shown in black and gray. The objects are ordered by the measured f_{esc}^{LyC} values as published in Flury et al. (2022a), which are also shown in the top left corner of each panel. The blue and red lines represent the position of $v = 0$ km s^{-1} for Mg II λ2796 and 2803, respectively.

upper limits, following Akritas & Siebert (1996). This leads to the probability of a spurious correlation, $p = 0.0216$, which confirms the strong trend. The former half of this trend is consistent with previous observations of strong LCEs (Izotov et al. 2022; Xu et al. 2022). Nonetheless, our sample is the first to show that this trend extends to non-LCEs, too. This can be explained because LCEs have more optically thin clouds in/around the galaxy than non-LCEs, so both the Mg II and LyC photons can escape with less absorption and scattering (Chisholm et al. 2022). This is also consistent with the expectations from simulations (Katz et al. 2022).

Notably, a high f_{esc}^{LyC} (=16.1%) was measured for galaxy J0917+3152, but its Mg II profiles also have clear absorption features. This can be explained by the high metallicity of J0917+3152, i.e., 12+log(O/H) = 8.46, which is the highest in our sample. Thus, for this object, there exist more magnesium atoms, given the same amount of hydrogen atoms. In this scenario, the clouds around J0917+3152 become optically thick to Mg II when it is still optically thin to LyC photons. Overall, the significant trend for the Mg II profiles from LCEs and non-LCEs is valid for galaxies with lower metallicity (in our case, 12+log(O/H) < 8.4). In these galaxies, the surrounding gas/clouds become optically thick to Mg II and LyC photons at similar depths (Chisholm et al. 2020).

3.2. Possible Geometry for the Escape of Mg II Photons and Constraints on Models

The escape of Mg II photons was first discussed in detail by Chisholm et al. (2020; hereafter, the "Chisholm model"—see their Section 6.4). This model assumes that the Mg II photons escape through a partial coverage geometry, which is

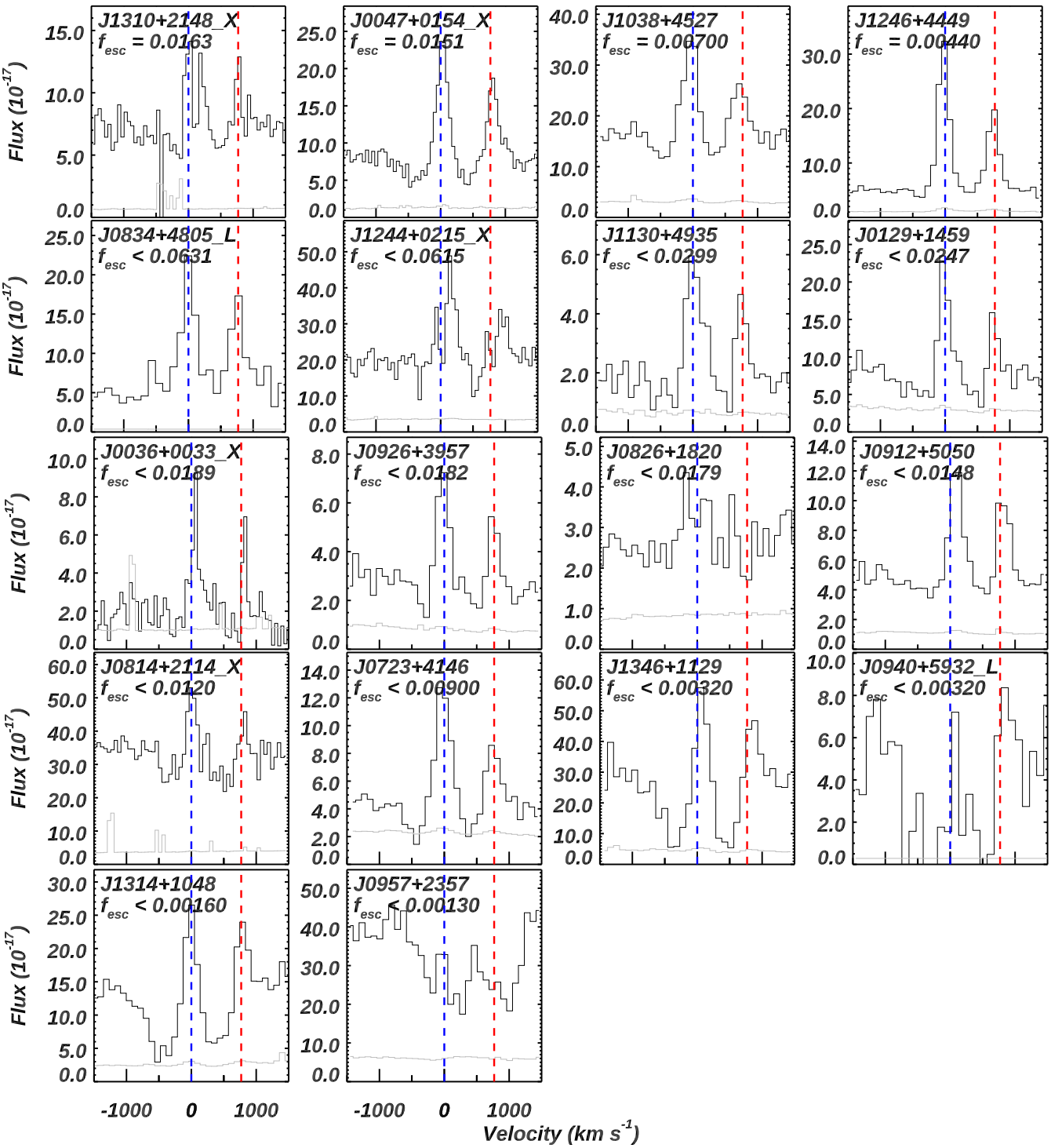

Figure 2. The same as Figure 1, but for the galaxies with lower f_{esc}^{LyC}. The upper limits of f_{esc}^{LyC} are presented for galaxies that have nondetections of LyC flux (Flury et al. 2022a). From the LCEs to non-LCEs, the Mg II line profiles show a clear transition from strong emission lines to P-Cygni profiles to strong absorption lines. See the further discussion in Section 3.1.

sometimes referred to as a "picket fence geometry" (see also Chisholm et al. 2018; Gazagnes et al. 2018; Saldana-Lopez et al. 2022; Xu et al. 2022):

$$f_{esc}^{\text{Mg II}} = \frac{F_{obs}}{F_{int}} = C_f(\text{Mg II})e^{-\tau_{thick}} + [1 - C_f(\text{Mg II})]e^{-\tau_{thin}}, \quad (1)$$

where F_{obs} and F_{int} are the observed and intrinsic flux of Mg II, respectively, C_f(Mg II) is the covering fraction for the optically thick paths of Mg II, and τ_{thick} and τ_{thin} are the optical depths for Mg II in optically thick and optically thin paths, respectively. In the optically thick paths, it is usually assumed that $\tau_{thick} \gg 1$, such that no Mg II photons are observed through

Table 2
Measurements from Optical Spectra for the Comparison Sample

Object (a)	O_{32} (b)	O/H (c)	F_{2796}^{Emi} (d)	F_{2803}^{Emi} (e)	$\lvert EW_{2796}^{Emi}\rvert$ (f)	$\lvert EW_{2803}^{Emi}\rvert$ (g)	$\lvert EW_{2796}^{Abs}\rvert$ (h)	$\lvert EW_{2803}^{Abs}\rvert$ (i)	Label (j)	f_{esc}^{MgII} (k)
J1033+6353	3.4	8.2	50.2 ± 7.0	34.9 ± 7.0	4.7 ± 0.8	3.6 ± 0.8	0.9 ± 0.3	0.0 ± 0.0	MgE	0.29 ± 0.04
J0917+3152	2.0	8.5	16.2 ± 7.4	13.5 ± 6.8	1.1 ± 0.4	0.9 ± 0.6	1.2 ± 0.4	0.9 ± 0.3	non-MgE	0.06 ± 0.03
J1327+4218	3.3	8.2	38.2 ± 4.4	22.7 ± 4.8	6.0 ± 0.6	4.1 ± 1.2	0.3 ± 0.08	0.5 ± 0.1	MgE	0.18 ± 0.02
J1410+4345	8.3	8.0	10.8 ± 2.4	7.8 ± 2.6	7.3 ± 1.6	5.6 ± 2.0	0.3 ± 0.09	0.0 ± 0.0	MgE	0.13 ± 0.03
J1158+3125	1.8	8.4	75.5 ± 5.2	38.6 ± 4.8	3.2 ± 0.2	1.7 ± 0.2	0.6 ± 0.2	0.3 ± 0.09	MgE	0.18 ± 0.01
J1235+0635	3.4	8.4	16.1 ± 1.6	10.6 ± 1.4	2.3 ± 0.2	1.5 ± 0.2	0.5 ± 0.1	0.0 ± 0.0	MgE	0.16 ± 0.02
J1248+1234	3.4	8.2	116.3 ± 5.0	62.3 ± 4.6	9.6 ± 0.6	5.0 ± 0.4	1.3 ± 0.4	0.5 ± 0.1	MgE	0.44 ± 0.02
J1517+3705	2.5	8.3	41.8 ± 1.2	26.7 ± 1.4	7.4 ± 0.4	4.2 ± 0.2	1.2 ± 0.2	0.7 ± 0.2	MgE	0.12 ± 0.003
J0122+0520	5.7	7.8	27.7 ± 2.6	17.5 ± 2.4	6.4 ± 1.0	4.8 ± 1.2	0.1 ± 0.03	0.3 ± 0.09	MgE	0.59 ± 0.06
J1301+5104	3.3	8.3	31.4 ± 5.6	16.4 ± 5.0	5.0 ± 0.8	3.1 ± 1.0	0.7 ± 0.2	0.3 ± 0.09	non-MgE	0.18 ± 0.03
J1648+4957	3.3	8.2	35.4 ± 0.4	23.9 ± 0.4	21.3 ± 0.2	16.1 ± 0.2	3.5 ± 0.2	0.0 ± 0.0	MgE	0.49 ± 0.006
J0911+1831	1.6	8.1	50.4 ± 7.4	34.4 ± 8.2	2.9 ± 0.4	2.0 ± 0.4	1.0 ± 0.3	0.5 ± 0.2	MgE	0.12 ± 0.02
J0113+0002	2.3	8.3	42.9 ± 3.0	23.1 ± 2.6	5.0 ± 0.6	2.9 ± 0.4	1.1 ± 0.3	0.5 ± 0.1	MgE	0.59 ± 0.04
J1133+4514	3.6	8.0	83.9 ± 6.4	43.1 ± 6.6	7.3 ± 0.6	3.8 ± 0.6	0.1 ± 0.04	0.0 ± 0.0	MgE	0.65 ± 0.05
J0811+4141	8.1	7.9	45.7 ± 4.2	28.0 ± 4.0	12.9 ± 1.2	7.4 ± 1.0	1.0 ± 0.3	0.0 ± 0.0	MgE	1.00 ± 0.23
J0958+2025	5.2	7.8	21.2 ± 5.0	8.4 ± 4.2	8.2 ± 2.6	4.4 ± 2.8	2.2 ± 0.7	0.5 ± 0.1	non-MgE	0.11 ± 0.03
J1310+2148	1.6	8.4	18.7 ± 2.0	12.4 ± 1.6	2.1 ± 0.4	1.4 ± 0.2	1.6 ± 0.5	0.3 ± 0.09	non-MgE	0.06 ± 0.007
J0047+0154	2.9	8.0	41.8 ± 2.8	31.0 ± 3.0	4.0 ± 0.2	3.1 ± 0.2	1.3 ± 0.2	0.8 ± 0.2	MgE	0.23 ± 0.02
J1038+4527	1.5	8.4	59.9 ± 8.4	35.4 ± 9.0	2.8 ± 0.4	1.7 ± 0.4	0.8 ± 0.2	0.6 ± 0.2	non-MgE	0.14 ± 0.02
J1246+4449	3.4	8.0	72.4 ± 4.2	41.4 ± 4.0	10.8 ± 0.6	6.2 ± 0.6	0.5 ± 0.2	0.1 ± 0.04	MgE	0.29 ± 0.02
J0834+4805	3.6	8.2	55.6 ± 1.4	44.7 ± 1.4	7.4 ± 0.4	6.1 ± 0.2	1.0 ± 0.2	0.0 ± 0.0	MgE	0.09 ± 0.002
J1244+0215	3.6	8.2	64.3 ± 7.6	40.4 ± 7.4	2.8 ± 0.6	1.8 ± 0.6	0.7 ± 0.2	0.5 ± 0.2	non-MgE	0.08 ± 0.009
J1130+4935	3.4	8.3	15.2 ± 2.0	7.4 ± 1.8	6.3 ± 0.8	3.1 ± 0.8	1.5 ± 0.4	0.9 ± 0.3	non-MgE	0.38 ± 0.05
J0129+1459	1.6	8.4	33.7 ± 7.6	15.8 ± 8.2	3.3 ± 0.8	1.7 ± 1.2	1.8 ± 0.5	1.2 ± 0.4	non-MgE	0.17 ± 0.04
J0036+0033	10.5	7.8	14.4 ± 2.2	7.5 ± 2.8	7.7 ± 1.8	5.3 ± 2.4	1.3 ± 0.4	1.0 ± 0.3	non-MgE	0.20 ± 0.03
J0926+3957	2.2	8.2	12.3 ± 2.2	6.1 ± 1.8	4.1 ± 0.8	1.8 ± 0.6	0.8 ± 0.3	1.0 ± 0.3	non-MgE	0.17 ± 0.03
J0826+1820	4.0	8.3	7.5 ± 2.6	3.4 ± 2.2	2.8 ± 1.0	1.8 ± 1.4	0.4 ± 0.1	1.2 ± 0.4	non-MgE	0.12 ± 0.04
J0912+5050	3.0	8.2	25.3 ± 3.2	19.6 ± 3.6	4.4 ± 0.6	3.5 ± 0.6	0.4 ± 0.1	0.1 ± 0.04	non-MgE	0.21 ± 0.03
J0814+2114	1.2	8.1	39.4 ± 9.2	28.7 ± 10.0	1.4 ± 0.4	0.9 ± 0.4	0.7 ± 0.2	0.3 ± 0.08	non-MgE	0.06 ± 0.01
J0723+4146	3.2	8.2	27.6 ± 6.4	16.9 ± 6.6	4.9 ± 1.2	3.6 ± 1.6	1.6 ± 0.5	0.9 ± 0.3	non-MgE	0.33 ± 0.08
J0940+5932	1.5	8.4	⋯	⋯	⋯	⋯	5.9 ± 0.2	4.2 ± 0.4	non-MgE	⋯
J1346+1129	1.1	8.3	72.1 ± 11.0	68.7 ± 12.8	2.3 ± 0.4	2.2 ± 0.6	2.6 ± 0.4	2.3 ± 0.4	non-MgE	0.11 ± 0.02
J1314+1048	1.1	8.3	25.0 ± 5.6	27.4 ± 8.0	1.4 ± 0.2	1.5 ± 0.6	3.0 ± 0.4	2.2 ± 0.4	non-MgE	0.05 ± 0.01
J0957+2357	0.5	8.4	⋯	⋯	⋯	⋯	2.9 ± 0.4	2.6 ± 0.4	non-MgE	⋯

Note. Measurements from the optical spectra for the galaxies in our sample. The galaxies are ordered by decreasing f_{esc}^{LyC}, as derived in Flury et al. (2022a; the same order as in Figures 1 and 2). Column (b): flux ratio between [O III] λ5007 and [O II] λ3727. Column (c): gas-phase metallicity in the form of 12+log(O/H). Columns (d) and (e): the measured emission line flux of the Mg II $\lambda\lambda$2796, 2803 lines in units of 10^{-17} ergs s^{-1} cm^{-2}, respectively. Columns (f) and (g): the measured rest-frame EW in units of Å for the emission part of the Mg II doublet (see Section 2.3). Columns (h) and (i): the measured rest-frame EW in units of Å for the absorption part of the Mg II doublet. Column (j): labels based on the Mg II line profiles, i.e., "MgE" = Mg II emitter, while "non-MgE" = Mg II nonemitter (see Section 3.2). Column (k): the derived escape fraction for Mg II λ2796 (see Section 3.3).

this path. In this model, Chisholm et al. (2020) also found that

$$R = \frac{F_{2796,obs}}{F_{2803,obs}} = 2e^{-\tau_{2803,thin}}, \quad (2)$$

where R is the emission line flux ratio between the Mg II doublet. This model has been shown to be successful in Chisholm et al. (2020) and Xu et al. (2022), for galaxies with strong Mg II emissions, where the Mg II photons escape from the galaxy through mostly optically thin paths. Furthermore, Katz et al. (2022) have tested this model in their hydro-cosmological simulations for EoR galaxy analogs. They find that the actual line-of-sight (LOS) f_{esc}^{MgII} match well with the predicted ones from the Chisholm model for galaxies with low metallicity (which are thus less dusty) and high f_{esc}^{LyC}. These galaxies have Mg II line profiles that are dominated by emission.

However, as described in Section 3.1, given the large dynamic ranges of our sample, by design, our galaxies have Mg II profiles ranging from strong emission to P-Cygni profiles and pure absorption. In the latter two cases, at least two factors complicate the applications of the Chisholm model: (1) the measurements of R from the spectra are not well defined, due to the absorption in the Mg II profiles, so the derived $\tau_{2803,thin}$ from R has large uncertainties; and (2) Mg II doublets are resonant lines, so the effect of the dust on Mg II lines is more substantial, which can cause strong absorption and scattering features in the spectra (e.g., J0957+2357). However, this effect cannot be described in simple terms, thus it is not included in the Chisholm model. Similarly, Katz et al. (2022) comment that the Chisholm model is likely inadequate for predicting f_{esc}^{MgII} for metal-rich (and therefore more dusty) galaxies in their simulations.

Currently, in this paper, in order to highlight the limitations of the Chisholm model, we manually split the galaxies in our

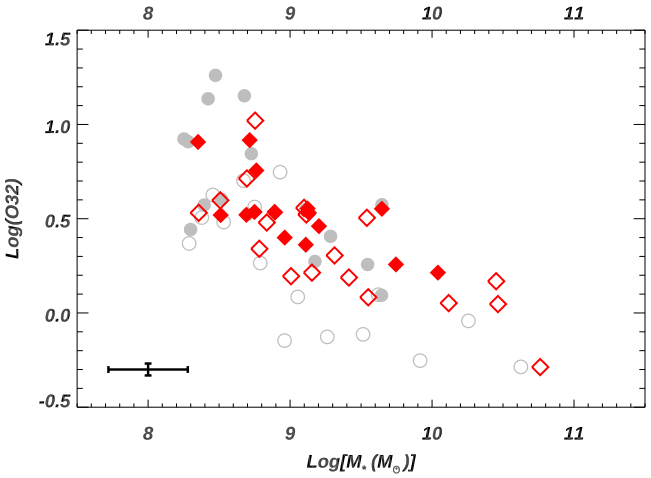

Figure 3. Comparison of the subsample studied in this paper (red) to the other galaxies in the LzLCS parent sample (gray; see Section 2). The gray solid and open symbols represent the galaxies from LzLCS, which are classified as LCEs and non-LCEs, respectively (Flury et al. 2022a). The red solid and open symbols represent the galaxies that are MgEs and non-MgEs, respectively (see the definitions in Section 3.2). The mean 1σ error bar is shown in the bottom left of the panel.

sample into two categories for our analyses. Those galaxies with Mg II as strong emission, minimal absorption, and symmetric line profiles are categorized as "MgEs" (an acronym for "Mg II emitters"), while the others are categorized as "non-MgEs." This subjective classification is similar to what was adopted in Katz et al. (2022). The Chisholm model should apply well to the former, since Mg II photons suffer few resonant scattering effects, but it should not apply perfectly to the latter. We show each galaxy's category in the penultimate column of Table 2. We further discuss how we handle these two categories in Section 4.2.

3.3. The Method for Estimating the Escape Fraction of Mg II

Henry et al. (2018) first introduced the understanding that one can derive the intrinsic flux of the Mg II from the correlation between Mg II/[O III] and [O III]/[O II] (hereafter, the "Henry model"):

$$R_{2796} = A_2 \times O_{32}^2 + A_1 \times O_{32} + A_0, \quad (3)$$

$$R_{2796} = \log(F_{\rm int}(\text{Mg II } \lambda2796)/F_{\rm int}([\text{O III}]\ \lambda5007))$$
$$O_{32} = \log(F_{\rm int}([\text{O III}]\ \lambda5007)/F_{\rm int}([\text{O II}]\ \lambda3727)), \quad (4)$$

where the emission line fluxes are all intrinsic, i.e., before the attenuation by dust and absorption in the LOS. Hereafter, we use $F_{\rm int}$ to denote the intrinsic flux. A_0, A_1, and A_2 are coefficients that are dependent on the gas-phase metallicity of the galaxy, but have little dependence on the ionization parameters and spectral slopes (Henry et al. 2018). Combining $F_{\rm int}$(Mg II) with the measured $F_{\rm obs}$(Mg II) from the spectra, one can derive $f_{\rm esc}^{\rm MgII}$.

The photoionization models in Henry et al. (2018) consider ionization-bounded (IB) geometry, where most of the cloud remains neutral and is optically thick to escaping photons. However, LCEs with strong Mg II emission lines can be partially density-bounded (DB; i.e., mostly optically thin), given the high O_{32} values that have been observed (e.g., Izotov et al. 2016a, 2016b, 2018a, 2018b, 2021; Flury et al. 2022a, 2022b; Xu et al. 2022). Thus, Xu et al. (2022) update the correlation coefficients of the Henry model to take into account the DB scenario. At a fixed metallicity, they also find that the different DB and IB models only move the correlation along the line defined in Equation (3). This should explain why Katz et al. (2022) find that the Henry model is a relatively good match to the galaxies in their simulations, but with moderate scatter, given the different metallicities of their simulated galaxies.

Given the derived $f_{\rm esc}^{\rm MgII}$, one can solve C_f(Mg II) and $\tau_{\rm thin}$ from Equations (1) and (2). Note that this requires robust measurements of the Mg II doublet flux ratio, i.e., R in Equation (2). As discussed in Section 3.2, this can be achieved in MgEs, but hardly in non-MgEs, due to the absorption features of Mg II. Since C_f(Mg II) and $\tau_{\rm thin}$ are then adopted to predict $f_{\rm esc}^{\rm LyC}$, accurate predictions are more difficult for non-MgEs (see the detailed discussions in Sections 3.4 and 4.2).

3.4. The Method for Predicting the Escape Fraction of LyC

As discussed in numerous previous publications (e.g., Zackrisson et al. 2013; Reddy et al. 2016; Chisholm et al. 2020; Kakiichi & Gronke 2021; Saldana-Lopez et al. 2022), the escape of LyC photons can be described as a partial coverage geometry:

$$f_{\rm esc}(\text{LyC}) = C_f(\text{H I})e^{-\tau_{\rm thick}} \times 10^{-0.4A_{\rm thick}} + [1 - C_f(\text{H I})]e^{-\tau_{\rm thin}} \times 10^{-0.4A_{\rm thin}}, \quad (5)$$

where C_f(H I) is the covering fraction for optically thick paths of H I, which are dominated by neutral gas, and $A_{\rm thick}$ and $A_{\rm thin}$ are the attenuation parameters for LyC photons in optically thick and optically thin paths, respectively.

For the galaxies in our LzLCS sample, Saldana-Lopez et al. (2022) have found that the covering fractions of lower-ionization lines (including O I, C II, and Si II) trace that of H I. Given the similar ionization potentials of Mg II to these lines, we adopt their best-fit linear correlation to estimate C_f(H I) as

$$C_f(\text{H I}) = (0.63 \pm 0.19)C_f(\text{Mg II}) + (0.54 \pm 0.09). \quad (6)$$

For optically thick paths, we assume that no LyC photons can escape (i.e., $\tau_{\rm thick}$ and/or $A_{\rm thick} \gg 1$). Therefore, the first term in Equation (5) is negligible. $A_{\rm thin}$ is related to the dust extinction at the LyC, for which we adopt the stellar extinction derived from the SED fittings in Saldana-Lopez et al. (2022). They used the Starburst99 template (Leitherer et al. 1999) and have assumed the extinction law from Reddy et al. (2015, 2016). Therefore, we can rewrite Equation (5) as

$$f_{\rm esc,pd}^{\rm LyC} = [1 - C_f(\text{H I})]e^{-N(\text{H I})\sigma_{\rm ph}} \times 10^{-0.4E(B-V)k(912)}, \quad (7)$$

where $f_{\rm esc,pd}^{\rm LyC}$ is the predicted absolute escape fraction of LyC, N(H I) is the column density of neutral hydrogen, $\sigma_{\rm ph}$ is the photoionization cross section of H I at 912 Å, $E(B-V)$ is the stellar dust extinction from Saldana-Lopez et al. (2022), and k (912) is the total attenuation curve at the Lyman limit. Given the Reddy et al. (2015, 2016) extinction law adopted in Saldana-Lopez et al. (2022), we have $k(912) = 12.87$. For other extinction laws, e.g., those of Cardelli et al. (1989) and Calzetti et al. (2000), $k(912) = 21.32$ and 16.62, respectively.

As shown in Chisholm et al. (2020) and Xu et al. (2022), by assuming that Mg II and LyC photons escape from similar optically thin paths, the column density of Mg II [i.e., N(Mg II)]

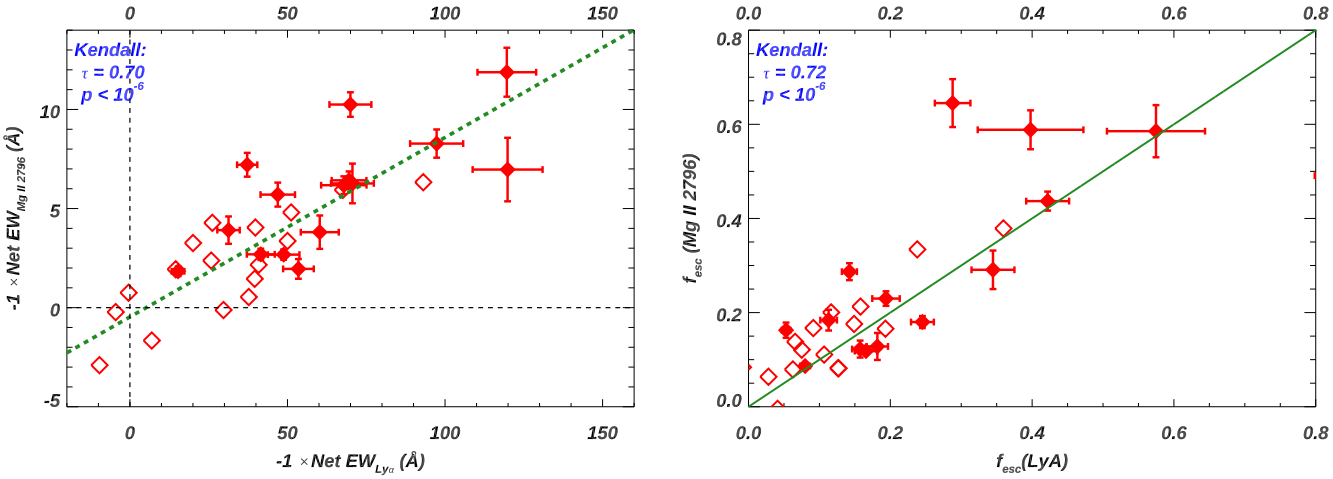

Figure 4. Correlations between the Mg II and Lyα properties. The galaxies from our sample that are labeled as MgE and non-MgE are shown by the solid and open symbols, respectively (Section 3.2). Left: the net EWs from Mg II λ2796 and Lyα are positively correlated. Each galaxy is shown as a dot, with the cross representing its error bars. The galaxies with strong Mg II emission lines are in the top right of the figure. The dashed green line represents the best linear fit. Right: the escape fractions of Mg II λ2796 and Lyα are tightly correlated. The correlation coefficients from the Kendall τ test are shown in the top left corner of each panel. The solid green line represents the 1:1 correlation. See the discussion in Section 4.1.

can be used to trace N(H I) over a large range, from DB to nearly IB regions:

$$N(\mathrm{H\ I}) = \alpha \times N(\mathrm{Mg\ II}), \tag{8}$$

where N(Mg II) can be calculated from the optical depth of Mg II, as inferred from R in Section 3.2, and $\alpha = \mathrm{N(Mg\ II)/N(H\ I)}$ is the column density ratio predicted from the CLOUDY models (Xu et al. 2022). α is dependent on the abundance ratio of [Mg/H] and the ionization, and has typical values $\sim 10^4$–10^5 for the galaxies in our sample. Combining Equations (5)–(8), we can calculate $f_{\mathrm{esc,pd}}^{\mathrm{LyC}}$, given the information of Mg II, metallicity, and dust.

In ~20 galaxies with strong Mg II emission lines, this model-predicted $f_{\mathrm{esc,pd}}^{\mathrm{LyC}}$ has been found to correlate well with the actual $f_{\mathrm{esc}}^{\mathrm{LyC}}$ measured from the spectra (Chisholm et al. 2020; Xu et al. 2022). Likewise, Katz et al. (2022) have also found that the $f_{\mathrm{esc,pd}}^{\mathrm{LyC}}$ correlates with the actual $f_{\mathrm{esc}}^{\mathrm{LyC}}$ for simulated high-redshift galaxies at different LOSs (the top middle panel of their Figure 17). But their correlation contains a large scatter. We note that they adopt α as the abundance ratio of hydrogen to oxygen, i.e., $\alpha = 46\frac{H}{O}$ (Chisholm et al. 2020). This assumes that the Mg II emission is found in neutral gas. This is not accurate, since known LCEs commonly have high O_{32} values, so at least a fraction of the interstellar medium (ISM; i.e., 1 - C_f(H I)) is DB. Thus, the Mg II in these galaxies should originate in regions where N(H II) is non-negligible. Our adopted α from the CLOUDY models in Equation (8) overcomes this problem (Xu et al. 2022). In Section 4.2, we compare the $f_{\mathrm{esc,pd}}^{\mathrm{LyC}}$ with the measured $f_{\mathrm{esc}}^{\mathrm{LyC}}$ from Flury et al. (2022a), based on the HST COS/G140L spectra and SED fittings.

4. Results

4.1. Estimates of the Escape Fraction of Mg II

From Sections 3.2 to 3.3, we show how to derive $f_{\mathrm{esc}}^{\mathrm{MgII}}$. The resulting values are listed in the final column of Table 2. Furthermore, in Figure 4, we present the correlations between Mg II and Lyα. In the left panel, we compare the net EW (i.e., the summed EW from both the emission and the absorption features) between Mg II and Lyα. To be consistent with the literature, we have multiplied the net EW by -1, allowing galaxies with strong emission lines to be in the top right corner and galaxies with strong absorption lines to be in the bottom left corner. We find a strong positive correlation between the net EWs of Mg II and Lyα. This is as expected, since both are resonant lines that should follow similar radiative transfer processes when traveling out of galaxies. The best-fit linear correlation is (shown as the dashed green line):

$$\begin{aligned} \text{net EW(Mg II)} &= a + b \times \text{net EW(Ly}\alpha\text{)} \\ a &= -0.468^{+0.157}_{-0.157} \\ b &= 0.091^{+0.003}_{-0.003}. \end{aligned} \tag{9}$$

Similar but less significant trends between EW(Mg II) and EW(Lyα) have also been published in Henry et al. (2018) and Xu et al. (2022), but they only focused on strong MgEs.

In the right panel of Figure 4, we compare the derived $f_{\mathrm{esc}}^{\mathrm{MgII}}$ with the escape fraction of Lyα ($f_{\mathrm{esc}}^{\mathrm{Ly}\alpha}$). The latter is derived from each galaxy's HST/COS spectra in Flury et al. (2022a). The correlation is significant ($p < 10^{-6}$), with scatter. We find that most of the galaxies follow the 1:1 correlation shown as the solid green line, which suggests $f_{\mathrm{esc}}^{\mathrm{Ly}\alpha} \simeq f_{\mathrm{esc}}^{\mathrm{MgII}}$. This is consistent with the results in Henry et al. (2018) and Xu et al. (2022), which also found that the $f_{\mathrm{esc}}^{\mathrm{MgII}}$ and $f_{\mathrm{esc}}^{\mathrm{Ly}\alpha}$ values were of the same order. This supports the scenario where Mg II and Lyα mainly escape from optically thin (or DB) holes in the ISM, likely in a single flight (e.g., Gazagnes et al. 2018; Chisholm et al. 2020; Saldana-Lopez et al. 2022). Thus, the path lengths of the Mg II and Lyα photons traveling out of the galaxy are similar, and the resulting escape fractions are close for both lines. One possible scenario is that there is zero dust in the optically thin paths. Future spatially resolved observations will be able to solve this puzzle. This includes our Lyα and Continuum Origins Survey (HST-GO 17069; PI: Hayes), which aims to spatially resolve the Lyα emission, dust, and stellar population for 41 of 66 LzLCS galaxies, using HST imaging.

For all the figures in this section, we show the Kendall τ coefficients and the probabilities of a spurious correlation

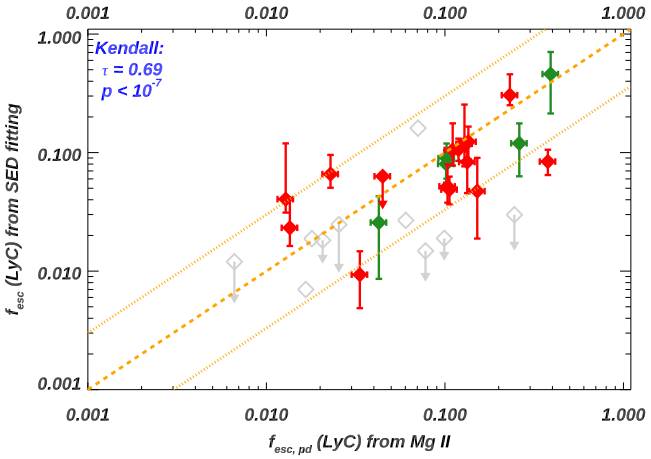

Figure 5. Comparison of the measured $f_{\rm esc}^{\rm LyC}$ with the predicted one from Mg II λ2796 emission lines. The galaxies that are labeled as MgE and non-MgE in our sample are represented by the solid red and open gray symbols, respectively (Section 3.2). The galaxies that are determined to be non-LCEs (Flury et al. 2022a) are shown as upper limits. The orange dotted lines show the factor-of-3 scatter around the 1:1 relationship (the dashed orange line). We also show five galaxies from Guseva et al. (2020) as the green symbols. See the discussion in Section 4.2

(p-values) in the top left corners. In the Kendall test, we have accounted for the upper limits (if any), following Akritas & Siebert (1996). We have also tested the correlations between the scatters in each figure with other galaxy properties, including metallicity, internal dust extinction, star formation rate surface density, and stellar mass. However, we do not find significant correlations.

4.2. Estimates of the Escape Fraction of LyC from Mg II

In Figure 5, we compare the $f_{\rm esc,pd}^{\rm LyC}$ derived in Section 3.4 with the $f_{\rm esc}^{\rm LyC}$ values derived from the HST/COS spectra (based on UV continuum fittings; Flury et al. 2022a). We draw the galaxies that are classified as MgE and non-MgE as solid and open symbols, respectively. We also include five galaxies from Guseva et al. (2020) that have high-quality VLT/X-Shooter observations as well as direct LyC measurements. We derive the $f_{\rm esc,pd}^{\rm LyC}$ in the same way as in Section 3.4, and we remeasure their $f_{\rm esc}^{\rm LyC}$ from HST/COS spectra, using the same methodology as in Flury et al. (2022a).

First of all, there is a strong correlation between the predicted $f_{\rm esc}^{\rm LyC}$ from the Mg II and the measured ones, given the probability of a spurious correlation $p < 10^{-7}$. This highlights the power of using Mg II to trace LyC. Given the scatter around the 1:1 relationship line (the dashed orange line), our predicted $f_{\rm esc}^{\rm LyC}$ values are accurate within a factor of 3. Considering only the non-MgEs (the open gray symbols), the correlation is less significant. This could be because their Mg II emission lines are affected by absorption features, and the derived $\tau_{2803,\rm thin}$ and C_f(Mg II) from Equation (2) are more uncertain.

For some of the non-MgEs, their Mg II spectra show significant resonant scattering or absorption signatures. These include galaxies showing double peaks in each of their Mg II emission lines (J1310+2148, J1244+0215, J0826+1820, and maybe J1235+0635) as well as galaxies showing strong absorption in Mg II (J0723+4146, J0940+5932, J1346+1129, J1314+1048, and J0957+2357). These galaxies should have optically thicker clouds in/around the galaxy, and our measurements of the emission line flux of Mg II are also uncertain. Thus, no meaningful predictions via Mg II emission lines can be made, and we have excluded these galaxies from Figure 5. We note that among these galaxies, only one (J1310+2148; $f_{\rm esc}^{\rm LyC} \sim 1.6\%$) has a small amount of LyC detected from the HST/COS spectra, while others show nondetections of LyC (see Figures 1 and 2). Thus, these non-MgEs are more similar to galaxies that are cosmologically irrelevant to the EoR ($f_{\rm esc}^{\rm LyC} \ll 1\%$). Therefore, precise estimates of their $f_{\rm esc}^{\rm LyC}$ are less important for our understanding of the SF galaxies contributing to the reionization. Furthermore, when selecting new LCEs for future observations, one can also exclude similar non-MgEs, based on the absorption and/or scattering features of the Mg II line profiles.

In the future, we plan to use detailed radiative transfer models to account for the escape of Mg II from the galaxy and to link it with the escape of Lyα and LyC (C. Carr et al. 2023, in preparation). We will then be able to model and separate the emission and absorption features from the observed Mg II spectra. This will be particularly helpful for making more realistic predictions of the $f_{\rm esc,pd}^{\rm LyC}$ for the galaxies that are labeled non-MgE.

Overall, our derived $f_{\rm esc,pd}^{\rm LyC}$ from the Mg II, metallicity, and dust can correctly trace the measured $f_{\rm esc}^{\rm LyC}$ within a factor of $\sim$3 for MgEs. This is consistent with the previous studies in Chisholm et al. (2020) and Xu et al. (2022). We conclude that Mg II emission lines, along with dust, can be used to predict the escape of LyC photons in MgEs, but we will need additional information to do so for non-MgEs (e.g., detailed radiative transfer models).

5. Conclusion and Future Work

We present analyses of Mg II spectra for 34 galaxies chosen from the LzLCS sample. These galaxies have published HST/COS data for their LyC and Lyα spectral regions, and we have obtained higher-S/N and higher-resolution spectra (than SDSS) for their Mg II regions.

While previous studies of Mg II in LCE candidates have only focused on MgEs, the galaxies in our sample have Mg II profiles ranging from strong emission to P-Cygni profiles to pure absorption. We find that there is a significant trend ($p = 0.0216$), with galaxies detected as strong LCEs showing larger EW(Mg II) in emission lines, while non-LCEs present larger EW(Mg II) in absorption.

We discuss the picket-fence geometry for the escape of the Mg II photons from galaxies. While this geometry has been found to apply well to galaxies that are categorized as MgEs, it has limitations in the case of non-MgEs. We then discuss how to use the CLOUDY photoionization models to help derive the escape fraction of Mg II ($f_{\rm esc}^{\rm MgII}$) from the optical spectra. For all the galaxies in our sample, we find that $f_{\rm esc}^{\rm MgII}$ correlates with the escape fraction of Lyα. We also show that the net EWs of Mg II and Lyα are tightly correlated for both MgEs and non-MgEs.

We also discuss the method for predicting the escape fraction of LyC ($f_{\rm esc,pd}^{\rm LyC}$) from measurements of Mg II, metallicity, and dust. We show that the predicted $f_{\rm esc,pd}^{\rm LyC}$ correlates well with the actual $f_{\rm esc}^{\rm LyC}$ derived from the HST/COS spectra, within a factor of $\sim$3. For non-MgEs, the correlation is less significant. This is because the absorption features in the Mg II spectra for non-MgEs complicate our measurements of the Mg II emission

lines. Additional information, e.g., from radiative transfer models, may help to solve this problem.

In the future, one could apply the Mg II correlations to various different studies, including the following. (1) We will perform detailed radiative transfer models to account for the escape of Mg II from the galaxy (C. Carr et al. 2023, in preparation). This will be especially helpful for non-MgE cases, where the clouds in/around the galaxy are not optically thin to Mg II. (2) For high-z galaxies, one could adopt the observed Mg II features to estimate the intrinsic amount of Lyα, which can be severely attenuated by the neutral IGM (e.g., Mason et al. 2018). Thus, with the aid of Mg II, one could obtain more accurate estimates of the IGM neutral fractions from Lyα. (3). One could conduct similar analyses of Mg II in higher-redshift LCE candidates, whose Mg II emission lines are shifted into the observable bands of the James Webb Space Telescope. The Lyα–Mg II correlations could be adopted to select LAEs that have detectable Mg II spectra, and the Mg II–LyC correlation could be used to predict the $f_{\rm esc}^{\rm LyC}$ in cases where the LyC cannot be directly detected.

X.X. and A.H. acknowledge support from the NASA STScI grant GO 15865. The observations reported here were obtained at the MMT Observatory, a joint facility of the University of Arizona and the Smithsonian Institution.

Support for this work was provided by NASA, through grant number HST-GO-15626 from the Space Telescope Science Institute. This research is based on observations made with the NASA/ESA Hubble Space Telescope, obtained from the Space Telescope Science Institute, which is operated by the Association of Universities for Research in Astronomy, Inc., under NASA contract NAS 5-26555. These observations are associated with programs 13744, 14635, 15341, 15626, 15639, and 15941. STScI is operated by the Association of Universities for Research in Astronomy, Inc., under NASA contract NAS 5-26555.

Based on observations collected at the European Organisation for Astronomical Research in the Southern Hemisphere, under ESO program 106.215K.001.

The Low-Resolution Spectrograph 2 (LRS2) was developed and funded by the University of Texas at Austin McDonald Observatory and the Department of Astronomy and by Pennsylvania State University. We thank the Leibniz-Institut für Astrophysik Potsdam (AIP) and the Institut für Astrophysik Göttingen (IAG) for their contributions to the construction of the integral field units.

A.S.L. acknowledges support from the Swiss National Science Foundation. H.A. is supported by CNES.

Facilities: HST (COS), MMT (Blue channel), APO (SDSS), VLT (X-Shooter), HET (LRS2).

Software: CLOUDY (v17.01, Ferland et al. 2017).

ORCID iDs

Xinfeng Xu https://orcid.org/0000-0002-9217-7051
Alaina Henry https://orcid.org/0000-0002-6586-4446
Timothy Heckman https://orcid.org/0000-0001-6670-6370
John Chisholm https://orcid.org/0000-0002-0302-2577
Rui Marques-Chaves https://orcid.org/0000-0001-8442-1846
Floriane Leclercq https://orcid.org/0000-0002-6085-5073
Danielle A. Berg https://orcid.org/0000-0002-4153-053X
Anne Jaskot https://orcid.org/0000-0002-6790-5125
Daniel Schaerer https://orcid.org/0000-0001-7144-7182
Gábor Worseck https://orcid.org/0000-0003-0960-3580
Ricardo O. Amorín https://orcid.org/0000-0001-5758-1000
Hakim Atek https://orcid.org/0000-0002-7570-0824
Matthew Hayes https://orcid.org/0000-0001-8587-218X
Zhiyuan Ji https://orcid.org/0000-0001-7673-2257
Göran Östlin https://orcid.org/0000-0002-3005-1349
Alberto Saldana-Lopez https://orcid.org/0000-0001-8419-3062

References

Akritas, M. G., & Siebert, J. 1996, MNRAS, 278, 919
Becker, G. D., D'Aloisio, A., Christenson, H. M., et al. 2021, MNRAS, 508, 1853
Begley, R., Cullen, F., McLure, R. J., et al. 2022, MNRAS, 513, 3510
Bergvall, N., Zackrisson, E., Andersson, B. G., et al. 2006, A&A, 448, 513
Bian, F., Fan, X., McGreer, I., Cai, Z., & Jiang, L. 2017, ApJL, 837, L12
Borthakur, S., Heckman, T. M., Leitherer, C., & Overzier, R. A. 2014, Sci, 346, 216
Bosman, S. E. I., Davies, F. B., Becker, G. D., et al. 2022, MNRAS, 514, 55
Boyett, K., Mascia, S., Pentericci, L., et al. 2022, ApJL, 940, L52
Calzetti, D., Armus, L., Bohlin, R. C., et al. 2000, ApJ, 533, 682
Cardelli, J. A., Clayton, G. C., & Mathis, J. S. 1989, ApJ, 345, 245
Chisholm, J., Prochaska, J. X., Schaerer, D., Gazagnes, S., & Henry, A. 2020, MNRAS, 498, 2554
Chisholm, J., Tremonti, C., & Leitherer, C. 2018, MNRAS, 481, 1690
Chisholm, J., Saldana-Lopez, A., Flury, S., et al. 2022, MNRAS, 517, 5104
Chonis, T. S., Hill, G. J., Lee, H., et al. 2016, Proc. SPIE, 9908, 99084C
de Barros, S., Vanzella, E., Amorín, R., et al. 2016, A&A, 585, A51
Dijkstra, M., Gronke, M., & Venkatesan, A. 2016, ApJ, 828, 71
Erb, D. K., Quider, A. M., Henry, A. L., & Martin, C. L. 2012, ApJ, 759, 26
Ferland, G. J., Chatzikos, M., Guzmán, F., et al. 2017, RMxAA, 53, 385
Finley, H., Bouché, N., Contini, T., et al. 2017, A&A, 605, A118
Fletcher, T. J., Tang, M., Robertson, B. E., et al. 2019, ApJ, 878, 87
Flury, S. R., Jaskot, A. E., Ferguson, H. C., et al. 2022a, ApJS, 260, 1
Flury, S. R., Jaskot, A. E., Ferguson, H. C., et al. 2022b, ApJ, 930, 126
Freudling, W., Romaniello, M., Bramich, D. M., et al. 2013, A&A, 559, A96
Gazagnes, S., Chisholm, J., Schaerer, D., Verhamme, A., & Izotov, Y. 2020, A&A, 639, A85
Gazagnes, S., Chisholm, J., Schaerer, D., et al. 2018, A&A, 616, A29
Gronke, M., Ocvirk, P., Mason, C., et al. 2021, MNRAS, 508, 3697
Guseva, N. G., Izotov, Y. I., Schaerer, D., et al. 2020, MNRAS, 497, 4293
Hayes, M. J., Runnholm, A., Gronke, M., & Scarlata, C. 2021, ApJ, 908, 36
Heckman, T. M., Sembach, K. R., Meurer, G. R., et al. 2001, ApJ, 558, 56
Henry, A., Berg, D. A., Scarlata, C., Verhamme, A., & Erb, D. 2018, ApJ, 855, 96
Henry, A., Scarlata, C., Martin, C. L., & Erb, D. 2015, ApJ, 809, 19
Inoue, A. K., Shimizu, I., Iwata, I., & Tanaka, M. 2014, MNRAS, 442, 1805
Izotov, Y. I., Chisholm, J., Worseck, G., et al. 2022, MNRAS, 515, 2864
Izotov, Y. I., Orlitová, I., Schaerer, D., et al. 2016a, Natur, 529, 178
Izotov, Y. I., Schaerer, D., Thuan, T. X., et al. 2016b, MNRAS, 461, 3683
Izotov, Y. I., Schaerer, D., Worseck, G., et al. 2018a, MNRAS, 474, 4514
Izotov, Y. I., Worseck, G., Schaerer, D., et al. 2021, MNRAS, 503, 1734
Izotov, Y. I., Worseck, G., Schaerer, D., et al. 2018b, MNRAS, 478, 4851
Jaskot, A. E., Dowd, T., Oey, M. S., Scarlata, C., & McKinney, J. 2019, ApJ, 885, 96
Ji, Z., Giavalisco, M., Vanzella, E., et al. 2020, ApJ, 888, 109
Kakiichi, K., & Gronke, M. 2021, ApJ, 908, 30
Katz, H., Garel, T., Rosdahl, J., et al. 2022, MNRAS, 515, 4265
Le Reste, A., Hayes, M., Cannon, J. M., et al. 2022, ApJ, 934, 69
Leitet, E., Bergvall, N., Hayes, M., Linné, S., & Zackrisson, E. 2013, A&A, 553, A106
Leitherer, C., Hernandez, S., Lee, J. C., & Oey, M. S. 2016, ApJ, 823, 64
Leitherer, C., Schaerer, D., Goldader, J. D., et al. 1999, ApJS, 123, 3
Marchi, F., Pentericci, L., Guaita, L., et al. 2017, A&A, 601, A73
Marchi, F., Pentericci, L., Guaita, L., et al. 2018, A&A, 614, A11
Marques-Chaves, R., Schaerer, D., Amorín, R. O., et al. 2022a, A&A, 663, L1
Marques-Chaves, R., Schaerer, D., Alvarez-Marquez, J., et al. 2022b, MNRAS, 517, 2972
Mason, C. A., Treu, T., Dijkstra, M., et al. 2018, ApJ, 856, 2
Mestrić, U., Ryan-Weber, E. V., Cooke, J., et al. 2020, MNRAS, 494, 4986
Naidu, R. P., Matthee, J., Oesch, P. A., et al. 2022, MNRAS, 510, 4582
Puschnig, J., Hayes, M., Östlin, G., et al. 2017, MNRAS, 469, 3252

Ramsey, L. W., Adams, M. T., Barnes, T. G., III, et al. 1998, Proc. SPIE, 3352, 34
Reddy, N. A., Steidel, C. C., Pettini, M., Bogosavljevic, M., & Shapley, A. E. 2016, ApJ, 828, 108
Reddy, N. A., Kriek, M., Shapley, A. E., et al. 2015, ApJ, 806, 259
Rivera-Thorsen, T. E., Hayes, M., & Melinder, J. 2022, A&A, 666, A145
Rivera-Thorsen, T. E., Dahle, H., Chisholm, J., et al. 2019, Sci, 366, 738
Robertson, B. E., Ellis, R. S., Furlanetto, S. R., & Dunlop, J. S. 2015, ApJL, 802, L19
Saldana-Lopez, A., Schaerer, D., Chisholm, J., et al. 2022, A&A, 663, A59
Schaerer, D., Izotov, Y. I., Verhamme, A., et al. 2016, A&A, 591, L8
Schenker, M. A., Ellis, R. S., Konidaris, N. P., & Stark, D. P. 2014, ApJ, 795, 20
Schlafly, E. F., & Finkbeiner, D. P. 2011, ApJ, 737, 103
Seive, T., Chisholm, J., Leclercq, F., & Zeimann, G. 2022, MNRAS, 515, 5556
Shapley, A. E., Steidel, C. C., Strom, A. L., et al. 2016, ApJL, 826, L24
Stark, D. P., Ellis, R. S., & Ouchi, M. 2011, ApJL, 728, L2
Steidel, C. C., Bogosavljević, M., Shapley, A. E., et al. 2018, ApJ, 869, 123
Vanzella, E., de Barros, S., Vasei, K., et al. 2016, ApJ, 825, 41
Vanzella, E., Nonino, M., Cupani, G., et al. 2018, MNRAS, 476, L15
Verhamme, A., Orlitová, I., Schaerer, D., & Hayes, M. 2015, A&A, 578, A7
Verhamme, A., Orlitová, I., Schaerer, D., et al. 2017, A&A, 597, A13
Vielfaure, J. B., Vergani, S. D., Japelj, J., et al. 2020, A&A, 641, A30
Wang, B., Heckman, T. M., Leitherer, C., et al. 2019, ApJ, 885, 57
Wang, B., Heckman, T. M., Amorín, R., et al. 2021, ApJ, 916, 3
Wang, W., Kassin, S. A., Faber, S. M., et al. 2022, ApJ, 930, 146
Weiner, B. J., Coil, A. L., Prochaska, J. X., et al. 2009, ApJ, 692, 187
Witstok, J., Smit, R., Maiolino, R., et al. 2021, MNRAS, 508, 1686
Worseck, G., Prochaska, J. X., O'Meara, J. M., et al. 2014, MNRAS, 445, 1745
Xu, X., Henry, A., Heckman, T., et al. 2022, ApJ, 933, 202
Zackrisson, E., Inoue, A. K., & Jensen, H. 2013, ApJ, 777, 39